

Discrete antiferromagnetic spin-wave excitations in the giant ferric wheel Fe₁₈

J. Ummethum,¹ J. Nehr Korn,² S. Mukherjee,³ N. B. Ivanov,^{1,4} S. Stui ber,² Th. Strässle,⁵
P. L. W. Tregenna-Pigott,⁵ H. Mutka,⁶ G. Christou,³ O. Waldmann,² and J. Schnack¹

¹*Fakultät für Physik, Universität Bielefeld, Postfach 100131, D-33501 Bielefeld, Germany*

²*Physikalisches Institut, Universität Freiburg, D-79104 Freiburg, Germany*

³*Department of Chemistry, University of Florida, Gainesville, Florida 32611, USA*

⁴*Institute of Solid State Physics, Bulgarian Academy of Sciences, Tzarigradsko chaussee 72, 1784 Sofia, Bulgaria*

⁵*Laboratory for Neutron Scattering, Paul Scherrer Institut, CH-5232 Villigen PSI, Switzerland*

⁶*Institut Laue-Langevin, 6 rue Jules Horowitz, BP 156, F-38042 Grenoble Cedex 9, France*

(Dated: June 28, 2012)

The low-temperature elementary spin excitations in the AFM molecular wheel Fe₁₈ were studied experimentally by inelastic neutron scattering and theoretically by modern numerical methods, such as dynamical density matrix renormalization group or quantum Monte Carlo techniques, and analytical spin-wave theory calculations. Fe₁₈ involves eighteen spin-5/2 Fe^{III} ions with a Hilbert space dimension of $\sim 10^{14}$, constituting a physical system that is situated in a region between microscopic and macroscopic. The combined experimental and theoretical approach allowed us to characterize and discuss the magnetic properties of Fe₁₈ in great detail. It is demonstrated that physical concepts such as the rotational-band or *L&E*-band concepts developed for smaller rings are still applicable. In particular, the higher-lying low-temperature elementary spin excitations in Fe₁₈ or AFM wheels in general are of discrete antiferromagnetic spin-wave character.

PACS numbers: 75.50.Xx, 75.10.Jm, 78.70.Nx

I. INTRODUCTION

Ring-like arrangements of a dozen or so of magnetic spins experiencing nearest-neighbor antiferromagnetic (AFM) exchange interactions, as realized experimentally for instance by the AFM molecular wheels, have attracted significant attention in the past decade.^{1–12} The molecular ferric wheel [Fe₁₈(pdH)₁₂(O₂CET)₆(NO₃)₆], or Fe₁₈ in short, is the largest magnetic molecular wheel synthesized to date.¹³ The molecule contains $N = 18$ Fe^{III} ions with spin $s = 5/2$, arranged in a ring-like fashion as shown in Fig. 1(a), and exhibits crystallographic C_6 symmetry. Its large yet finite size makes it an ideal candidate to explore the region between microscopic and macroscopic physics (the system is mesoscopic). The magnetism in the Fe₁₈ wheel was studied before using high-field magnetic torque measurements, and the low-lying energy spectrum up to 2 meV was investigated by inelastic neutron scattering (INS).¹⁴ The experimental data demonstrated the dynamics of the Néel vector, and the magnetic torque provided direct evidence for quantum oscillations in the Néel vector tunneling gap due to quantum phase interference.¹⁴

The experimental observations have been well described in terms of an effective two-sublattice Hamiltonian, which had been demonstrated before for smaller wheels with up to 10 spin sites to approximate well the low-energy part of the true spectrum.^{15,16} This Hamiltonian is in fact related to the more general concept of the *L&E*-band picture, which describes the elementary excitations as a set of rotational (parabolic) energy bands, and which was shown to apply to a variety of AFM spin clusters with bipartite or tripartite sublattice structure.^{10,15–19} The effective Hamiltonian allowed

a description of the experiments because it operates in a Hilbert space of dimension 2116 (for Fe₁₈), which can easily be handled on a personal computer using standard numerical diagonalization techniques. However, direct confirmation of its applicability to wheels as large as Fe₁₈ is lacking and important magnetic parameters such as magnetic anisotropy could not be determined reliably. Furthermore, higher-lying spin excitations, which are expected in the *L&E*-band concept, were not observed.

The numerically exact evaluation of all energy eigenvalues and eigenfunctions of a giant molecule such as Fe₁₈ poses a great challenge for theory since the size of the related Hilbert space grows as $(2s + 1)^N$ and for Fe₁₈ assumes a value of 101,559,956,668,416 $\approx 10^{14}$. This dimension is much too big for a matrix diagonalization. Even a decomposition of the Hamiltonian matrix according to the available symmetries, as successfully done for the smaller AFM wheels such as CsFe₈ or Fe₁₀,^{20–23} is not efficient enough to ease the problem. Fortunately, the magnetic molecule Fe₁₈ is non-frustrated, which permits the application of Quantum Monte Carlo (QMC) methods,^{24–26} and furthermore is quasi one-dimensional, which makes it ideal for (Dynamical) Density Matrix Renormalization Group (DDMRG & DMRG) calculations.^{27–32} The first method allows the evaluation of thermodynamic observables such as the magnetic susceptibility whereas the second delivers transition rates between low-lying energy levels that can be related to the INS spectrum.

In this work a comprehensive study of the higher-lying excitations in Fe₁₈, which in the language of the *L&E*-band concept correspond to the *E* band or discrete spin-wave excitations, is reported. Experimentally the excitation spectrum was determined by high-energy INS

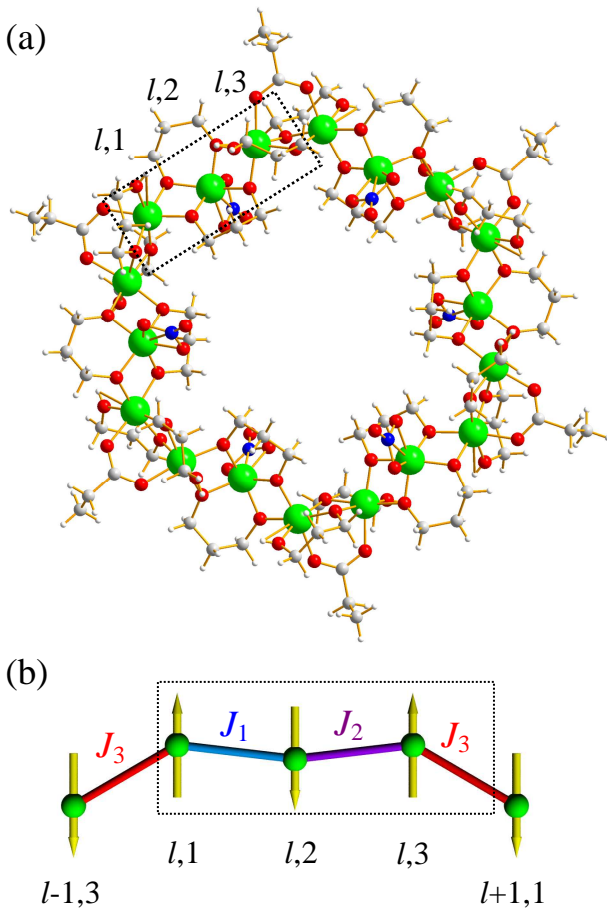


FIG. 1: (Color online) (a) Ball-and-stick representation of the molecular structure of the Fe_{18} molecule (Fe: green, O: red, N: blue, C: gray, and H: white). The dashed box indicates the unit cell used for magnetic modeling, see next panel. (b) Unit cell (dashed box) and labeling of the spin sites (text at bottom) used for the theoretical calculations as suggested by the symmetry of the molecule. The exchange constants J_1 , J_2 , and J_3 associated to different bonds are indicated.

measurements extending the energy range to 13.5 meV, and the temperature-dependent magnetic susceptibility, which probes the full energy spectrum. Theoretically, the QMC and DDMRG techniques were used to reproduce the experimental magnetic susceptibility and INS data with excellent accuracy. Because of the size and the structure of Fe_{18} the DDMRG calculations are time-consuming, which prevents a systematic scanning of the magnetic parameter space or least-squares fit approaches. This problem was circumvented by resorting to spin-wave theory as an intermediate step. This allowed us to refine the microscopic spin Hamiltonian for Fe_{18} and deduce accurate microscopic magnetic parameters. A key result is that the spin-wave like character of the higher lying excitations is preserved although the refined Hamiltonian is less symmetric compared to the assumptions in Ref. 14. Furthermore, the validity of the $L&E$ -band concept is confirmed for Fe_{18} .

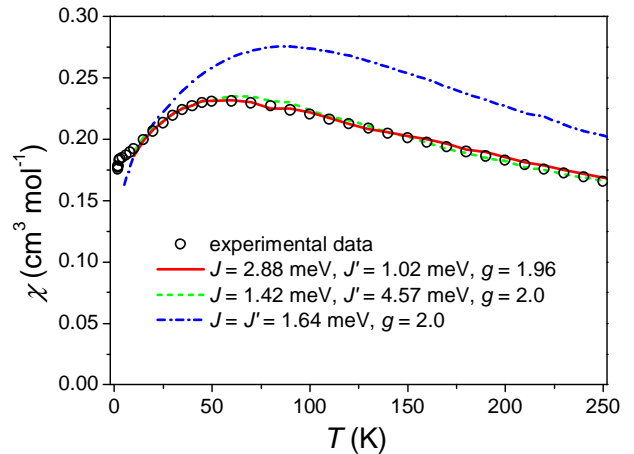


FIG. 2: (Color online) Experimental (open circles) and simulated (lines) magnetic susceptibility as function of temperature. The three simulated curves were obtained from the microscopic model Eq. (1) using QMC. The parameters in the simulations are as indicated (with $J_1 = J_2 = J$ and $J_3 = J'$).

The article is organized as follows: It begins with a discussion of the experimental results for the susceptibility and the INS cross section in Sec. II. This is followed by a theoretical analysis in Sec. III and a discussion in Sec. IV. After our final conclusions further details of the employed methods are given in an appendix.

II. EXPERIMENTAL RESULTS

The experimental methods used for sample preparation, and magnetic susceptibility and INS measurements are described in Appendix A 1. Figure 2 shows the magnetic susceptibility χ as function of temperature measured on a poly-crystalline sample. At 250 K, a χ value of $0.17 \text{ cm}^3/\text{mol}$ is observed, which increases with decreasing temperature, reaches a maximum of $0.23 \text{ cm}^3/\text{mol}$ at a temperature of ca. 50 K, and decreases further with decreasing temperature. At the lowest temperature an abrupt decrease is observed. Such a behavior is typical for AFM molecular wheels,² and the data are consistent with earlier measurements on a micro-crystalline sample.¹³ The ground state of an even-membered AFM wheel is a total spin singlet, $S = 0$, and the susceptibility is hence expected to approach zero at zero temperature, which is not observed here because in large wheels the drop to $\chi = 0$ occurs only at the lowest temperatures (the gap to the first excited triplet is roughly given by $\sim 4J/N$ and is small in Fe_{18}) and the susceptibility in this temperature regime is strongly affected by the presence of magnetic anisotropy (which is significant in Fe_{18}).³³ The solid curves are theoretical results which are discussed below.

The INS spectrum recorded at an incoming wavelength of $\lambda = 4.2 \text{ \AA}$ and a temperature of 1.9 K on the spectrometer IN5 is shown in Fig. 3. At low energies a strong

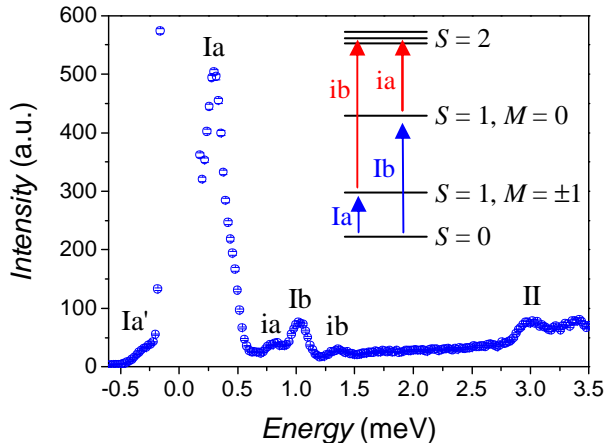


FIG. 3: Experimental INS spectra recorded on IN5 with incoming neutron wavelength $\lambda = 4.2 \text{ \AA}$ at 1.9 K. Positive energy transfer corresponds to neutron energy loss. The labels indicate observed transitions. The inset sketches the assignment of the low-energy excitations as inferred previously.¹⁴

feature at 0.3 meV (peak Ia) together with its corresponding anti-Stokes feature (peak Ia') is observed. At around 1 meV a group of three features appears, peak ia at 0.8 meV, peak Ib at 1 meV, and peak ib at 1.36 meV. These transitions were already observed in the previous low-energy INS experiment¹⁴ and interpreted as follows: Peaks Ia and Ib correspond to cold magnetic transitions from the $S = 0$ ground state to the first excited $S = 1$ multiplet, which is zero-field split by magnetic anisotropy into its components $M = \pm 1$ and $M = 0$, and peaks ia and ib were identified as hot magnetic transitions from this first excited $S = 1$ multiplet to the next-higher lying $S = 2$ multiplet (see inset to Fig. 3). In addition to these transitions, a further peak II at 3.0 meV is observed.

Figure 4(a) presents the INS spectra recorded with an incoming wavelength $\lambda = 3.2 \text{ \AA}$ on the spectrometer FOCUS. In the 1.5 K data a prominent feature at 3 meV is observed on the neutron-energy loss side, which obviously corresponds to peak II found before in the IN5 data (Fig. 3). Also, a shoulder near the elastic line at ca. 1 meV is observed, which obviously corresponds to peak Ib (peak ib is not detected here because of its weak intensity and the lower experimental resolution in the $\lambda = 3.2 \text{ \AA}$ experiment). Two further features are observed, a very weak feature at ca. 2 meV and a weak broad feature at ca. 4.5 meV. The spectrum recorded at 75 K shows, apart from a strongly increased background due to the excited lattice, no clear features. It is therefore reasonable to assume that at this temperature predominantly the lattice excitations are observed, and the magnetic scattering intensity is distributed over all energies. The lattice contribution (on the neutron-energy loss side) at low temperatures may thus be estimated by scaling the 75 K data with the Bose factor $[1 - \exp(-E/k_B T)]^{-1}$, which determines the temperature dependence of phononic scattering. The esti-

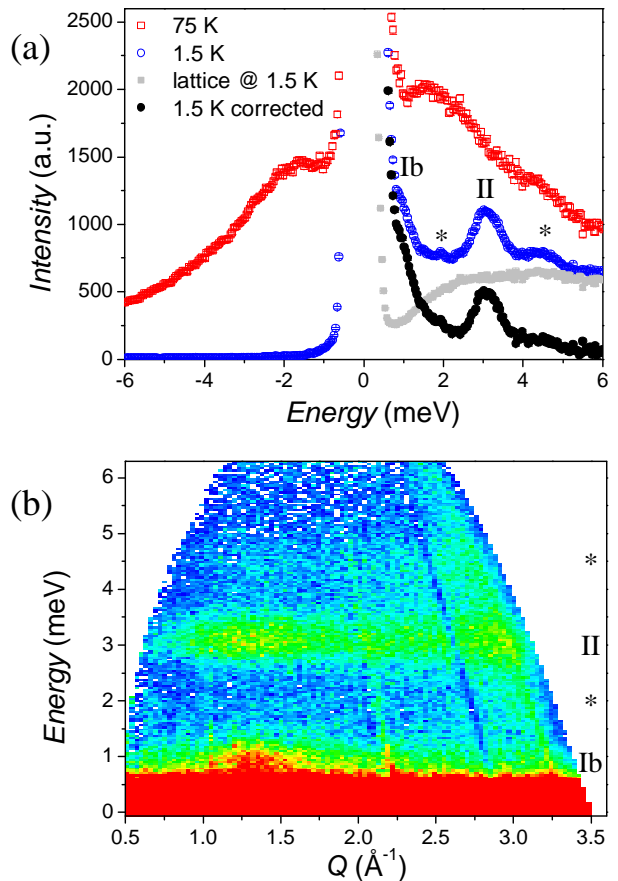


FIG. 4: (Color online) (a) Experimental INS spectra recorded on FOCUS with incoming neutron wavelength $\lambda = 3.2 \text{ \AA}$ at 1.5 K (blue open circles) and 75 K (red open squares). The 75 K data were Bose-scaled to yield the estimated lattice scattering at 1.5 K (gray solid squares) and were subtracted from the 1.5 K data yielding the Bose-corrected data (black solid circles). (b) $S(Q, \omega)$ plot of the (not Bose-corrected) 1.5 K data shown in panel (a). Intensity is color-coded from blue (low intensity) to red (high intensity). The labels indicate observed transitions, and the asterisks spurious features as discussed in the text. Positive energy transfer corresponds to neutron energy loss.

mated lattice contribution is then subtracted from the low-temperature INS data, a procedure we call Bose correction. This approach was used with considerable success in the past.^{18,34,35} In the Bose-corrected 1.5 K data, shown also in Fig. 4(a), peak II remains strong, providing a strong hint that it is of magnetic origin.

Also the dependence of the INS intensity on momentum transfer Q could be studied, which often allows for an unambiguous conclusion as regards the origin of INS features. The $S(Q, \omega)$ plot of the 1.5 K data is shown in Fig. 4(b). Peaks Ib and II are clearly identified, which is impressive considering that a non-deuterated molecular powder sample was measured at high energies. Magnetic and phononic excitations may be clearly differentiated by their Q dependence, since for the former the intensity is

either strongest at low Q values or typically is maximal at around 1.2 \AA^{-1} ,³⁶ while for the latter an increase of the intensity with Q^2 is expected.³⁷ Clearly, the intensity of both peaks Ib and II is negligible at low Q and passes through a maximum between 1.1 and 1.5 \AA^{-1} . At higher Q values the observed intensity is almost constant. Such a Q dependence is characteristic for the magnetic excitations in AFM molecular wheels.^{10,18,33,38–41} Hence, on the basis of the temperature dependence, the Bose correction, and the Q dependence peaks Ib and II are clearly magnetic. In contrast, the features at 2 meV and 4.5 meV do exhibit their strongest intensity at large Q values, and are hence safely assigned to spurious and/or lattice contributions, which for the 2 meV feature is also confirmed by its absence in the $\lambda = 4.2 \text{ \AA}$ data, Fig. 3.

The INS spectra recorded on FOCUS with incident wavelength $\lambda = 2.26 \text{ \AA}$ at 1.5 and 75 K are displayed in Fig. 5(a). In the 1.5 K spectrum peak II at ca. 3 meV is again observed. Furthermore, prominent features are also observed at around 8.5 meV (peak III) and 12 meV (peak IV), and at ca. 6 meV a weak feature is found. Peak III is significantly broader than the experimental resolution, and appears to consist of two features. The 75 K spectrum exhibits an increased intensity reflecting the strong phononic scattering intensity, and no detailed features are observed at the lower energies. However, two features are present at energies roughly corresponding to those of peaks III and IV. A Bose correction was applied to the 1.5 K data as discussed before yielding the Bose-corrected 1.5 K data shown in Fig. 5(a). Both peaks III and IV are pronounced in the Bose-corrected data, which strongly hints towards a magnetic origin of this scattering intensity. The right shoulder at ca. 9 meV on the high-energy side of feature III in the (original) 1.5 K data is significantly reduced by the Bose-correction, which suggests a lattice origin of this scattering intensity. The $S(Q, \omega)$ plot of the 1.5 K spectrum is given in Fig. 5(b). The peaks II, III, and IV are clearly present and exhibit strong scattering intensity at low Q values, with indications of a maximum below 1.5 \AA^{-1} , which unambiguously demonstrates their magnetic origin. At all energies a significant phonon contribution is observed at the largest Q values. To gain further insight into the nature of the weak feature at ca. 6 meV , the INS data were analyzed via Q slices, as shown in Fig. 5(c). The 6 meV feature is better detected in the Q slices the higher the Q values are, and appears to be essentially absent in the Q slice with the lowest Q values. It is hence assigned to a spurious or lattice feature. In contrast, the peaks II, III, and IV are more pronounced in the lower Q slices, again demonstrating their magnetic origin.

To summarize the INS findings, besides the four low-energy features Ia, Ib, ia, and ib, which were already observed before in previous INS experiments,¹⁴ three further cold magnetic transitions II, III, and IV were observed in the high-energy regime up to 14 meV . An analysis of these transitions using Gaussian fits with sloped background yielded the energy positions as peak II:

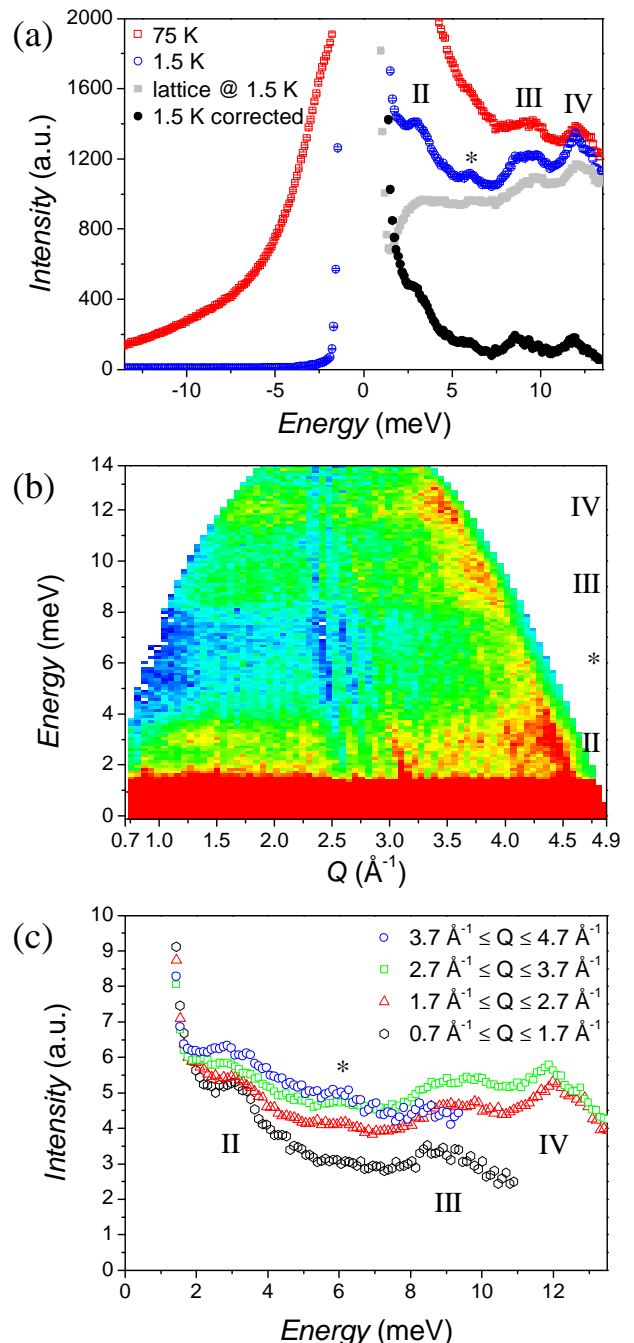


FIG. 5: (Color online) (a) Experimental INS spectra recorded on FOCUS with incoming neutron wavelength $\lambda = 2.26 \text{ \AA}$ at 1.5 (blue open circles) and 75 K (red open squares). The 75 K data were Bose-scaled to yield the estimated lattice scattering at 1.5 K (gray solid squares) and were subtracted from the 1.5 K data yielding the Bose-corrected data (black solid circles). (b) $S(Q, \omega)$ plot of the (not Bose-corrected) 1.5 K data shown in panel (a). Intensity is color-coded from blue (low intensity) to red (high intensity). (c) Q -sliced 1.5 K data, with the Q slices as indicated. The labels indicate observed transitions and the asterisk a spurious feature as discussed in the text. Positive energy transfer corresponds to neutron energy loss.

3.0(1) meV, peak III: 8.5(2) meV, peak IV: 12.0(2) meV.

III. ANALYSIS

A. Spin model for Fe₁₈

The generic Hamiltonian for the description of the magnetic properties of a molecular wheel of $N = 18$ Fe^{III} spins is a Heisenberg Hamiltonian with nearest-neighbor interactions plus a term reflecting the single-ion anisotropy of the Fe^{III} ions.¹⁴ In principle, this would lead to at least 36 unknown parameters. However, Fe₁₈ possesses a crystallographic C_6 symmetry axis perpendicular to the wheel plane, which leads to a repeating unit of three Fe^{III} ions, as indicated in Fig. 1(b). Therefore, the Heisenberg part of the Hamiltonian can be formulated with at most three different exchange constants:

$$\hat{H}_H = \sum_{l=1}^{L=6} J_1 \hat{\mathbf{S}}_{l,1} \cdot \hat{\mathbf{S}}_{l,2} + J_2 \hat{\mathbf{S}}_{l,2} \cdot \hat{\mathbf{S}}_{l,3} + J_3 \hat{\mathbf{S}}_{l,3} \cdot \hat{\mathbf{S}}_{l+1,1}, \quad (1)$$

where $L = N/3$ is the number of unit cells and l enumerates the repeating units and has to be understood modulo L [for the enumeration of the individual spin sites see also Fig. 1(b)].

The magnetic susceptibility, Fig. 2, is compatible with a non-magnetic, total spin $S = 0$ ground state. In addition, the high temperature behavior of χ requires that the sum of all exchange interactions is antiferromagnetic.⁴² Considering the susceptibility function further, one can even conclude that all couplings along the ring have to be antiferromagnetic because if any of the exchange interactions were ferromagnetic, either the ground state would possess a total spin of $S = 15$ or the susceptibility would rise to much larger values at low temperatures than observed. Hence, we can safely restrict our analysis to AFM exchange interactions, $J_1, J_2, J_3 > 0$. A closer look at the structure of the molecule suggests the simpler model where $J_2 = J_3 = J$ and $J_1 = J'$, since the exchange bridges connecting the centers $\hat{S}_{l,1}$ to $\hat{S}_{l,2}$ and $\hat{S}_{l,2}$ to $\hat{S}_{l,3}$ are chemically identical and structurally very similar, while the bridge connecting centers $\hat{S}_{l,3}$ to $\hat{S}_{l+1,1}$ is chemically very different (see Fig. 1). In the following we will denote the uniform ring with $J_1 = J_2 = J_3 = J$ as a one- J model, the situation with $J_2 = J_3 = J$ and $J_1 = J'$ as a two- J model, and the general case of three different exchange constants as a three- J model.

The interaction with an applied magnetic field \mathbf{B} is described by the Zeeman Hamiltonian

$$\hat{H}_Z = g\mu_B \sum_{j=1}^{N=18} \hat{\mathbf{S}}_j \cdot \mathbf{B}, \quad (2)$$

where the g factor is close to 2 for Fe^{III} ions, j enumerates the individual spin sites, and μ_B is the Bohr magneton.

Previous results suggest that the single-ion anisotropy of the Fe^{III} ions, which is modeled by the term

$$\hat{H}_D = D \sum_{j=1}^{N=18} (\hat{S}_j^z)^2, \quad (3)$$

is relatively small in magnitude yet strongly affects the spin dynamics at very low energies.¹⁴ However, it is expected to have negligible effect on the excitations at higher energies.¹⁸ Therefore this term is not included in our analysis, but this assumption is carefully checked and confirmed in Sec. III C.

In order to determine the exchange parameters we approach the relevant energy spectrum in three steps: In a first step we analyze the spin-wave excitations and compare them with the observed INS excitations in order to narrow down the range of possible parameter values and to qualitatively understand the character of the excitations. This approach is motivated by the L & E -band picture, which connects the higher-energy low-temperature excitations to discrete spin-waves, and spin-wave theory was indeed able to reproduce the excitations in the AFM wheel CsFe₈ with semi-quantitative accuracy.¹⁸ In a second step we perform large-scale DDMRG calculations for quite a number of parameter sets that yield model parameters of high accuracy. Finally, these are compared with QMC calculations of the magnetic susceptibility.

B. Spin-wave calculations

The one-magnon excitations of Hamiltonian Eq. (1) can be obtained in the framework of standard spin-wave theory (SWT).⁴³ Some modification of the theory becomes inevitable, however, when studying physical quantities such as the dynamical correlation function in Eq. (A3), which exhibits divergencies caused by the Goldstone modes. The gapped structure of these modes in finite Heisenberg clusters and AFM wheels in particular can be handled within the framework of SWT by introducing chemical potentials for the spin sites, yielding the so-called modified SWTs.^{44–52} We will come back to this point in Sec. IV. Here we calculate the one-magnon spectrum of Eq. (1) in a linear SWT approximation; for details we refer to Appendix C.

The spin-wave excitation energies of the Fe₁₈ system are displayed in Fig. 6(a) as a function of a shift quantum number k , which arises from Fourier transforming the periodic ring of L unit cells (physically it would correspond to a wavevector only in the infinite chain). For comparison, as guides to the eye, the dispersions of the spin-wave branches of a large ($L = 300$) ring are also shown. Three branches $\omega_1(k)$, $\omega_2(k)$, $\omega_3(k)$ are observed as expected from the three centers in the unit cell. For Fe₁₈ the k values are restricted to the discrete values $k = 0, \pm\frac{1}{9}\pi, \pm\frac{2}{9}\pi, \frac{1}{3}\pi$, and a discrete excitation spectrum with 17 energy states is obtained [$\omega_1(0)$ is the ground state]. The excitations fall into four energy levels E_1 ,

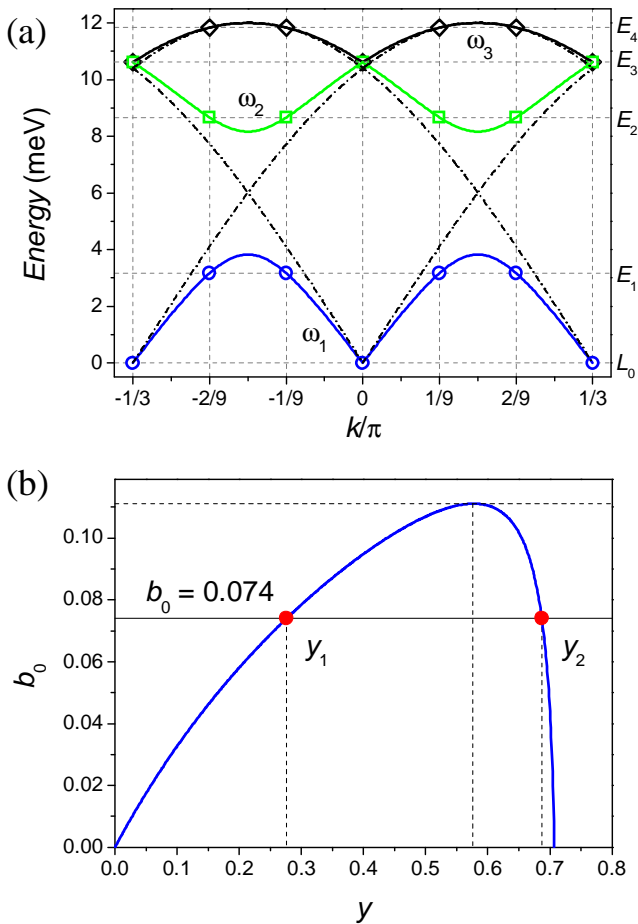


FIG. 6: (Color online) (a) Spin-wave excitation spectrum of Hamiltonian Eq. (1) with $L = 6$ (symbols) and $L = 300$ (solid curves) as obtained from SWT for the parameter $b_0 = 0.074$. The energy levels E_1 to E_4 are defined by Eq. (C15). The dashed-dotted curves display the spectrum for the one- J model. (b) Dependence of Eq. (4) for $J_1 = J_2 = J$ and $J_3 = J'$ on the scaling variable y . The two solutions $y_1 = 0.276$ and $y_2 = 0.687$ for $b_0 = 0.074$ corresponding to $J'/J \approx 3$ and $J'/J \approx 0.3$, respectively, are indicated. Both solutions produce identical one-magnon spectra.

E_2 , E_3 , and E_4 (each is four-fold degenerate because of the symmetries in the SWT approximation). The level L_0 is formed by the Goldstone mode $\omega_1(k = \pi/3)$, which has zero energy in the standard SWTs. It acquires a gap however when modified SWTs are used, which in the quantum spectrum relates to the gap between the $S = 0$ ground state and first excited $S = 1$ multiplet (singlet-triplet gap). Within the $L&E$ -band concept the energies in the levels E_1 to E_4 correspond to the E band, and the ground state and $k = \pi/3$ mode to the L band.¹⁶ The dispersions for the uniform ring or one- J model are also displayed in Fig. 6(a) for comparison (J was chosen here such that the maximal energy coincides).

The SWT calculations allow some useful insight. A modulation of the exchange constants away from uniform opens a gap between the branches $\omega_1(k)$ and $\omega_2(k)$,

which in relative terms shifts E_1 down and E_2 up. As shown in Appendix C, SWT implies three relations between the reduced energies E_1/E_3 , E_2/E_3 and E_4/E_3 , which depend only on the dimensionless parameter b_0 ,

$$b_0 = \frac{3J_1^2 J_2^2 J_3^2}{(J_1 J_2 + J_2 J_3 + J_3 J_1)^3}. \quad (4)$$

Detailed inspection shows that the difference between the energy levels E_3 and E_4 does of course vary with varying exchange constants, but always remains relatively small, and it turns out that it is always significantly too small to account for the experimentally observed energy difference of peaks III and IV. Finally, the relation $E_1 + E_2 = E_4$ follows from the first two equations in Eq. (C18). The conclusion from all this is that even in the most general case of three different exchange couplings, the possible variation in the relative energies of the levels is restricted. In particular, the three- J model does not introduce significantly more flexibility in adjusting the energies as compared to the two- J model, despite the additional free parameter. Intuitively this is reasonable, since the main characteristics which govern the dispersions in Fig. 6(a) is the maximal energy (or E_4) and the size of the gap between the energies E_1 and E_2 . This strongly suggests that the possible small differences between the exchange constants J_1 and J_2 cannot be resolved in the present experiments, and that therefore the two- J model is appropriate for Fe_{18} .

Comparing the spin-wave spectrum with the experimental INS peaks, it is obvious that the level E_1 corresponds to peak II (peaks Ia and Ib are related to the singlet-triplet gap or level L_0 , which in the present SWT calculation is obtained at zero energy). However, at higher energies SWT predicts three further levels while only two INS peaks III and IV are observed. This results in several possibilities for the assignment, which could all be ruled out because of discrepancies with experiment except one, namely the assignment that E_2 corresponds to peak III and E_4 to peak IV. According to SWT an excitation corresponding to level E_3 between peaks III and IV is expected but not observed. This problem will be resolved by the DDMRG calculations discussed in the next subsection, which additionally provides scattering intensities.

Due to the restrictions for the energies mentioned before (cf. Appendix C), a perfect mapping of the spin-wave spectrum onto the positions of the above three INS peaks is not possible even in the general case of three exchange parameters. A good approximation to the INS peaks can however be obtained with the two- J model, which is also compatible with the chemical structure of Fe_{18} . A least-squares fit resulted in the optimal parameter $b_0 = 0.074$, which yields the energy levels $E_1 = 3.17$ meV, $E_2 = 8.67$ meV, $E_3 = 10.61$ meV, and $E_4 = 11.84$ meV, which for E_1 , E_2 , and E_4 can be compared to the INS energies peak II = 3.0 meV, peak III = 8.5 meV, and peak IV = 12.0 meV. The good agreement suggests that the exchange constants obtained from

this analysis should provide excellent starting values for a more refined analysis.

In fact, from Eq. (4), for any fixed value of b_0 there are two different pairs of exchange constants which produce identical one-magnon spectra (in the two- J model). The dependence of b_0 on the scaling variable $y = J_2/\sqrt{J_1^2 + J_2^2 + J_3^2}$ is presented in Fig. 6(b), and the graphical solution of Eq. (4) for the optimal parameter $b_0 = 0.074$ is also shown. The two solutions correspond to $J'/J \approx 3$ and $J'/J \approx 0.3$, which in the following will be referred to as the $J' > J$ and $J' < J$ scenario, respectively. DDMRG considered in the next subsection allows us to disentangle these two cases.

It is finally mentioned that a good approximation to the experimental spectrum cannot be achieved by a uniform ring or the one- J model, see also Fig. 6(a). The two- J model is thus both the minimal and appropriate model for Fe_{18} . This is in accordance with similar findings for another, but structurally similar Fe_{18} spin ring.⁴

C. DDMRG analysis of the experimental data

In the first part of this section, the magnetic susceptibility and high-energy INS (peaks II-IV) data are analyzed. The single-ion anisotropy term is neglected and only the Heisenberg Hamiltonian Eq. (1) is used. In the second part, using the low-energy INS data (peaks Ia and Ib) the magnitude and influence of the single-ion anisotropy term Eq. (3) are investigated.

Using DDMRG³⁰⁻³² (see Appendices A 2 and B) the INS intensities were first calculated for the one- J model. The calculated peaks correspond to transitions from the $S = 0$ ground state to excited states with $S = 1$, and occur approximately at $0.27J$, $2.0J$, $3.6J$, $4.8J$, and $5.5J$. Therefore, as already deduced from SWT, it is not possible to find a single J for which more than two INS peaks can be reproduced. Furthermore, simulations of the magnetic susceptibility (see Fig. 2) are in marked discrepancy with experiment. The one- J model is hence disregarded for interpreting the magnetism in Fe_{18} . This model will however be helpful for the discussion of the general physics in AFM molecular wheels in Sec. IV.

Simulations of the magnetic susceptibility for the two- J model (Fig. 2) showed that for both the $J' > J$ and $J' < J$ scenarios the experimental data can be excellently reproduced. The simulations are in fact not very sensitive to small variations of the exchange constants, as long as their average remains constant.⁴² Using the information from the SWT calculations and magnetic susceptibility simulations extensive DDMRG calculations for several (J, J') parameter sets were performed that aimed at fitting the high-energy INS data. The broadening $\eta = 0.5$ meV (cf. Appendix A 2) was chosen such that in the DDMRG calculation the FWHM of the Lorentzian peaks approximately corresponds to the experimental resolution (1.1 meV for the $\lambda = 2.26$ Å INS measurements). For small parameter variations (and for not too

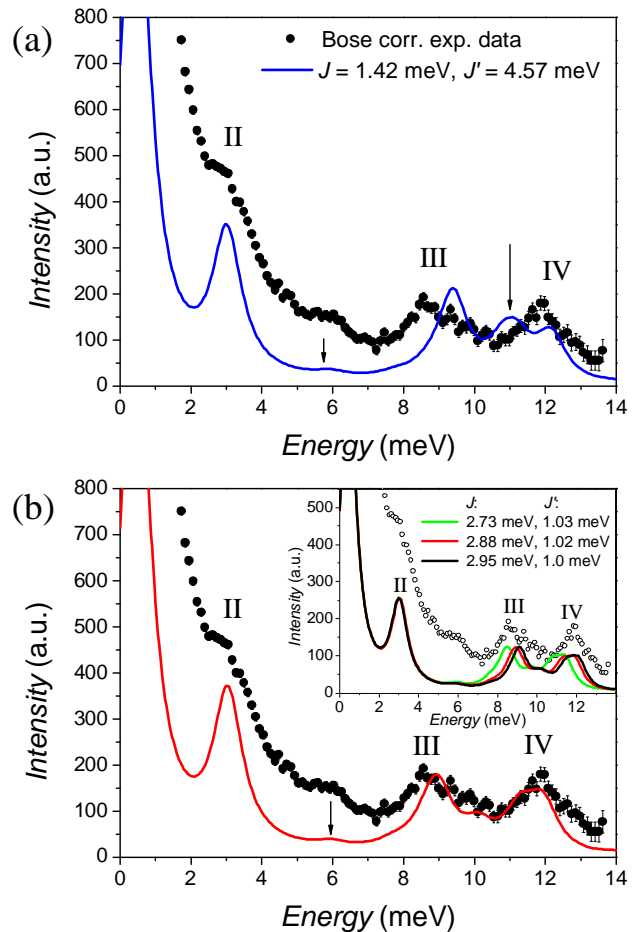


FIG. 7: (Color online) INS spectra as obtained by DDMRG calculations (solid lines) and comparison to the experimental Bose-corrected data (solid and open circles) deduced from the $\lambda = 2.26$ Å, 1.5 K INS run. (a) Best-fit simulation for the $J' > J$ scenario, with exchange parameters $J = 1.42$ meV, $J' = 4.57$ meV. The arrows indicate features in the simulated spectrum discussed in the text. (b) Best-fit simulation for the $J' < J$ scenario, with exchange parameters $J = 2.88$ meV, $J' = 1.02$ meV. The inset shows simulated INS spectra for three slightly different exchange constants used to infer the errors in the determined exchange constants.

small a difference between J and J') the following qualitative results were obtained [cf. Fig. 7(b)], which for brevity will be discussed for the $J' < J$ scenario (for the $J' > J$ scenario interchange J and J'):

(1) A variation of J' while keeping J constant affects the complete spectrum, but the peak positions depend approximately linearly on J' .

(2) Variation of J with constant J' mainly shifts the peaks above 6 meV without changing the relative positions of those peaks, i.e., the "bandwidth" of the high-energy part above 6 meV is not significantly changed. The positions and heights of the peaks below 6 meV are almost unaffected by variation of J .

These findings are in accordance with the SWT results. Using these trends for the $J' > J$ scenario, the

best agreement with experiment was obtained for $J = 1.42$ meV and $J' = 4.57$ meV [Fig. 7(a)]. Five prominent peaks are observed in the DDMRG spectrum at the energies of ca. 0.43, 3.0, 9.4, 10.9, and 12.1 meV (which can in fact contain some nearly degenerate transitions, which are not resolved due to the finite broadening η). The calculated spectrum is compared with the Bose-corrected INS spectrum recorded at a wavelength of 2.26 Å in Fig. 7(a). The agreement with the experimental peak III could probably be further optimized by fine-tuning of J and J' . However, in the DDMRG spectra an additional peak at about 11 meV is observed, marked by an arrow in Fig. 7(a), which obviously corresponds to the spin-wave level E_3 discussed in the preceding subsection. It is, however, not seen in the experiment, which disfavors the $J' > J$ scenario as a model for the magnetism in Fe₁₈.

Further efforts therefore concentrated on the $J' < J$ scenario. Here also five peaks are observed in the DDMRG spectra at ca. 0.43, 3.0, 8.9, 10.1, and 11.6 meV. However, the intensity of the peak at 10.1 meV, which relates to the spin-wave level E_3 , is relatively weak. The best agreement of the DDMRG spectra with the experimental high-energy data was obtained for $J = 2.88$ meV and $J' = 1.02$ meV. The agreement is in fact very good, see Fig. 7(b), and in particular considerably better than for the $J' > J$ scenario [Fig. 7(a)]. The errors of the determined exchange constants were estimated to ~ 0.15 meV for J and ~ 0.05 meV for J' . These estimates are based on the variation of the peak positions for varied parameters [cf. inset to Fig. 7(b)]. The smaller error for J' stems from the fact that the experimental position of peak II has been measured more precisely than the positions of peaks III and IV, and the position of the simulated peak II is mainly determined by this coupling constant. Within these error bounds, it is possible to match the positions of all experimental high-energy peaks in the DDMRG simulation. The magnetic susceptibility is also reproduced excellently with these exchange parameters.

The consideration of a non-zero but small temperature in the simulations would not change the positions of the main peaks, but would change their heights a bit. Additional hot peaks resulting from transitions from excited states would also appear, but because of the singlet-triplet gap of about 0.3 meV, which should be compared to the temperature of 1.5 K at which the high-energy INS data were obtained, the ground state population is estimated to be larger than 90 %. Hence, transitions from the ground state clearly dominate, and comparing the zero-temperature DDMRG and 1.5 K experimental spectra is justified.

Interestingly, the DDMRG spectra for both scenarios produce a very weak scattering intensity at ca. 6 meV (indicated in Fig. 7 by arrows), where a weak feature is indeed observed in the experiment. The analysis of the experimental data in Sec. II suggested that this intensity is of non-magnetic origin. In view of the DDMRG results,

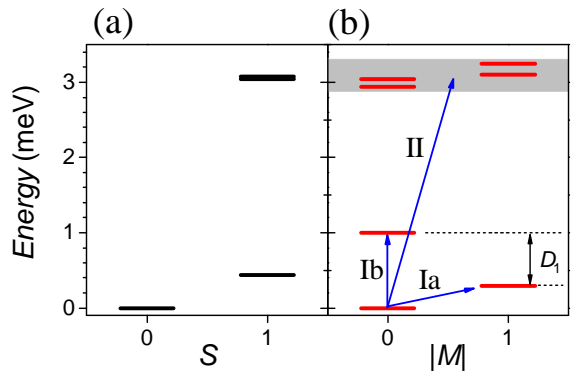


FIG. 8: Calculated low-energy spectrum for $J = 2.88$ meV, $J' = 1.02$ meV as obtained using DMRG with multiple target states. (a) Energy spectrum for $D = 0$ as function of total spin S . (b) Energy spectrum for $D = 0.03$ meV as function of the magnitude of the magnetic quantum number M , showing the ZFS of the $S = 1$ multiplets. For the lowest $S = 1$ multiplet the ZFS is determined by D_1 . The gray box is centered at the center of gravity of the higher-lying multiplets and has a height corresponding to the experimental resolution (430 μ eV) of the data shown in Fig. 4. The ZFS of the lowest $S = 1$ multiplet is 0.7 meV and much larger than the splitting of the next two, nearly degenerate multiplets, which is 0.3 meV, and smaller than the experimental resolution. The observed cold INS transitions are indicated by arrows.

it could be possible that this feature is, at least in parts, i.e., at low momentum transfer Q , due to magnetic scattering. The present experiments, however, cannot resolve this issue.

In a next step the influence and magnitude of the single-ion anisotropy term, Eq. (3), are analyzed. Peaks Ia and Ib, observed at energies of 0.3 meV and 1.0 meV in the $\lambda = 4.2$ Å INS experiment and in a previous work,¹⁴ were assigned to the transitions from the $S = 0$ ground state to the first excited $S = 1$ multiplet, which exhibits a Zero-Field Splitting (ZFS) due to the single-ion anisotropy of the Fe^{III} ions which can be characterized by an anisotropy constant D_1 [see Fig. 8(b)]. The relation between D and D_1 was estimated in Ref. 14 by extrapolating results on smaller wheels, but the accuracy remained unclear, and therewith the accuracy of the deduced value of D in Fe₁₈. Therefore we used the ALPS DMRG code²⁶ to calculate the lowest-lying energies for $\hat{H} = \hat{H}_H + \hat{H}_D$. For $J = 2.88$ meV, $J' = 1.02$ meV, and $D = 0.030$ meV the low-lying energies reproduced excellently the transition energies observed for peaks Ia and Ib. Based on parameter variations in the calculations and the widths of the experimentally observed peaks, we estimate the error in D to be ~ 5 μ eV.

The comparison of the energy level structure with and without \hat{H}_D in Fig. 8 shows that the anisotropy-induced splitting is largest for the first $S = 1$ multiplet but much smaller for the next two (nearly degenerate) $S = 1$ multiplets. This is in agreement with findings on e.g. the CsFe₈ wheel.¹⁸ This is a clear indication that the effect

of the single-ion anisotropy on the higher-lying excitations studied in this work can be neglected: The position of the center of gravity is nearly unaffected and the splitting is smaller than experimental resolution. It is mentioned that the center of gravity is not equal to the “center of INS intensity” since the INS intensity is generally distributed unequally among the excitations.

To summarize this section, the experimental magnetic susceptibility and INS data for Fe₁₈ can very well be reproduced with the microscopic parameters $J = 2.88(15)$ meV, $J' = 1.02(5)$ meV, and $D = 0.030(5)$ meV [$J = 33(2)$ K, $J' = 11.8(6)$ K, $D = 0.35(6)$ K]. Alternative exchange parameters were extensively searched for but found to provide inferior agreement with experiment.

IV. DISCUSSION

According to the *L&E*-band picture, the low-temperature excitations in even-membered AFM wheels fall into two energy regimes with different character. For the wheels Cr₈ and CsFe₈ this scenario was confirmed both experimentally and theoretically in detail,^{10,18} but for Fe₁₈ the picture has been incomplete so far. For Fe₁₈, the *L*-band excitations at the lowest energies were experimentally investigated in detail in the previous study Ref. 14 by means of low-energy INS (peaks Ia, Ib in Fig. 3) and ultra-low-temperature high-field magnetization and magnetic torque measurements. The *E*-band or the higher-lying elementary excitations accessible at low temperatures were carefully studied in the present work. However, different models were used in the interpretation of the low-energy and high-energy data, and their relation is considered now.

The low-energy experimental data¹⁴ could be described extremely well by the effective two-sublattice Hamiltonian

$$\hat{H}_{AB} = j\hat{\mathbf{S}}_A \cdot \hat{\mathbf{S}}_B + d \left[(\hat{S}_A^z)^2 + (\hat{S}_B^z)^2 \right], \quad (5)$$

where $\hat{\mathbf{S}}_A$ and $\hat{\mathbf{S}}_B$ represent the total spins of length $S_A = S_B = Ns/2$ on each of the two sublattices *A* and *B*, and with appropriate effective exchange constant j and anisotropy d . This simple two-spin Hamiltonian is suggested by the *L&E*-band picture, and was established as an effective low-energy approximation of the uniform ring (one-*J*) model with an additional anisotropy, or $\hat{H}_{uni} = \hat{H}_H + \hat{H}_D$ with $J_1 = J_2 = J_3 = J$.⁵³ The magnetic parameters are related through $j = a_1 J$ and $d = b_1 D$, where the coefficients a_1 and b_1 depend strongly on N and s . The underlying assumption is that the eigenstates of \hat{H}_{uni} in the low-energy sectors are well approximated by “quasi-classical” spin states of the form $|S_A S_B S M\rangle$ (with $S_A = S_B = Ns/2$). Within this space \hat{H}_{uni} is equivalent to \hat{H}_{AB} in first order, yielding $a_1 = a_1^{AB}$ with $a_1^{AB} = 4/N$ and $b_1 = b_1^{AB}$ with $b_1^{AB} = (2s - 1)/(Ns - 1)$. However, quantum corrections modify these parameters significantly, which can be

accounted for by matching the low-energy states to the exact energy spectrum, if the latter is available, yielding values a_1^{qm} and b_1^{qm} .⁵³ For $N = 18$, $s = 5/2$ relevant for Fe₁₈, $a_1^{qm} = 0.2721$ was extracted from QMC calculations,⁵⁴ and $b_1^{qm} \approx 0.07$ was determined by extrapolating results of rings with lengths of up to $N = 10$.^{14,53} Using these results $J = 1.64$ meV and $D = 0.026$ meV was inferred for Fe₁₈ from the low-energy data in Ref. 14.

We recalculated the parameters a_1^{qm} and b_1^{qm} as follows: a_1^{qm} was determined from the singlet-triplet gap of the Heisenberg part of \hat{H}_{uni} since it can be obtained very accurately by DMRG. For the estimation of b_1^{qm} the spectra of \hat{H}_{uni} and \hat{H}_{AB} were compared for different values of b_1 and D using DMRG and exact diagonalization codes of the ALPS package.^{26,55} Our results are $a_1^{qm} = 0.2683(1)$ and $b_1^{qm} = 0.063(2)$. Hence, the refined magnetic parameters $J = 1.64(3)$ meV and $D = 0.029(1)$ meV are obtained, with which \hat{H}_{uni} describes very well the experimental low-energy excitations in Fe₁₈.

The susceptibility and high-energy INS data, however, cannot be reproduced by a uniform ring model as demonstrated in Sec. III C. The two-*J* model was required. From the susceptibility simulations two equally good parameter sets were found (one with $J' < J$ and one with $J' > J$). Based on susceptibility it was not possible to prefer one set over the other. Also, spin-wave theory predicted no differences between these two models regarding the excitation energies. The simulation of the high-energy INS data using DDMRG revealed differences between these two models, and favored the $J' < J$ model (Fig. 7).

Also for the three-*J* model, or $\hat{H} = \hat{H}_H + \hat{H}_D$ with general exchange couplings, the effective two-sublattice Hamiltonian \hat{H}_{AB} is obtained in first-order as the effective low-energy approximation. The modulations in the exchange (and anisotropy) constants along the wheel are effectively averaged out in the *L*-band states,⁵⁶ suggesting the average exchange constant $J = (J_1 + J_2 + J_3)/3$. However, the parameter a_1 is strongly modified. Indeed, for the $J' < J$ and $J' > J$ models determined in this work the average exchange constants are $J = 2.26$ meV and 2.47 meV, while for the uniform ring model $J = 1.64$ meV (all three models yield identical low-energy spectra, e.g. energies for peaks Ia and Ib). It is interesting to observe that the parameter b_1 is comparatively less affected; for the models here $D = 0.030(5)$ meV is deduced while the uniform ring model yielded $D = 0.029(1)$ meV, which agree within the errors.

The energy spectra of the elementary excitations are compared for the $J' < J$, $J' > J$, and uniform ring models in Fig. 9, where only the Heisenberg parts were considered ($D = 0$). Also, the spin-wave energies as predicted by our SWT (Appendix C) are indicated. Apparently, the lowest-lying triplet, which belongs to the *L* band, has identical energy in all three models (as necessitated by experiment). Furthermore, the next-higher

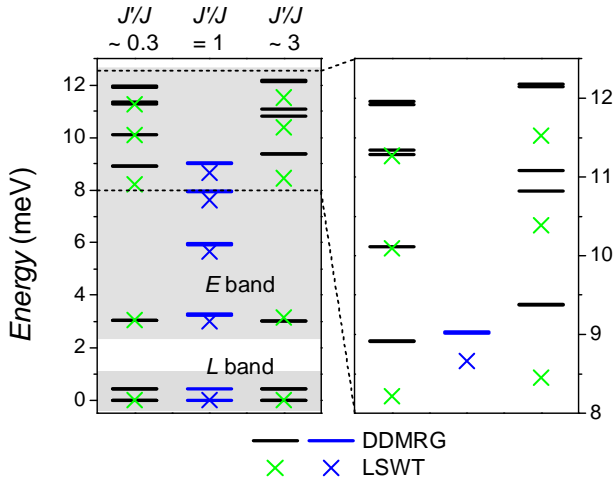


FIG. 9: (Color online) Effect of different coupling constants in the Fe_{18} wheel. The left panel shows the ground state and the excitations in the one-magnon energy sector for the three models $J = 2.88$ meV, $J' = 1.02$ meV ($J'/J \approx 0.3$), $J = J' = 1.64$ meV, and $J = 1.42$ meV, $J' = 4.57$ meV ($J'/J \approx 3$). The bars represent the energies as obtained from DDMRG calculations, and the crosses the results of LSWT. The LSWT excitation energies were calculated using Eq. (C15) (see Appendix C). The right panel shows a zoom into the high-energy region.

lying triplet state, corresponding to the energy level E_1 or peak II, which belongs to the E band, is produced at nearly identical energies in all models. The main difference is in the further higher-lying states of the E band. In the one- J model their "bandwidth" of ca. 2.5 meV is obtained approximately correctly, but is predicted at significantly too low an energy. Hence, the key experimental signature for modulated exchange couplings in Fe_{18} is the large energy gap between peaks II and III. Notably, for all three models the simple LSWT can reproduce the DDMRG excitation energies in the E band semi-quantitatively. This strongly suggests that these excitations do indeed correspond to discrete AFM spin-wave excitations. The lowest-lying singlet-triplet gap or L band is not reproduced by the LSWT (i.e. is calculated zero energy) by reasons discussed before in Sec. III B.

Finally, the excitations of the uniform Heisenberg ring shall be considered in detail by comparing the results of (D)DMRG calculations to those of various SWTs. The discussion parallels that in Ref. 18 for the AFM wheel CsFe_8 with $N = 8$, $s = 5/2$. AFM systems with disordered ground states, such as the AFM wheels, represent a challenge for any SWT since these start by construction from an ordered ground state. As a result, the energies of the Goldstone modes are obtained as zero even in finite spin systems, and divergencies appear e.g. in the magnetization (which actually can be used as an indication of the absence of order in the considered spin model^{43,44}). Linear and interacting SWT (LSWT and ISWT) are typical representatives.^{44,45} These drawbacks

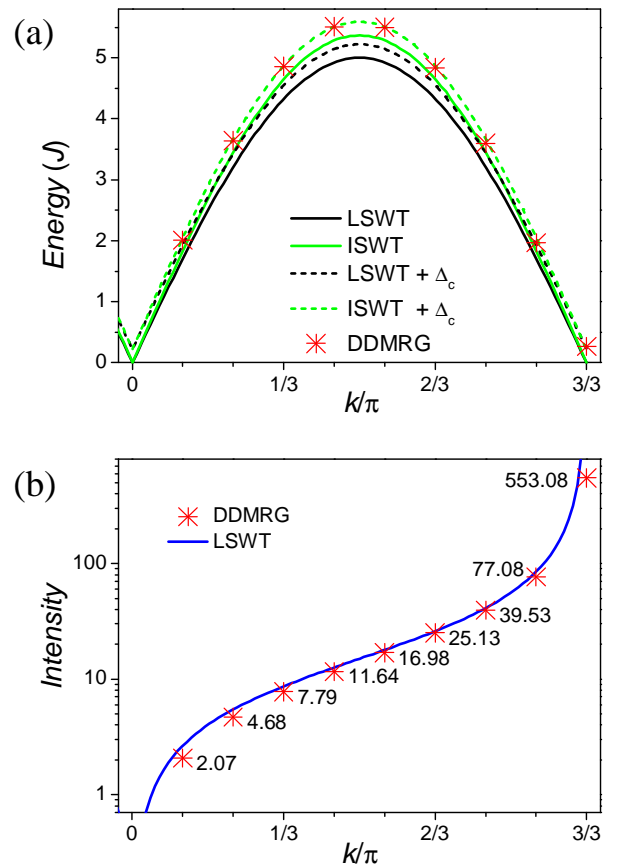


FIG. 10: (a) Dispersion of the one-magnon excitations of the uniform Heisenberg ring (one- J model) as obtained by DDMRG calculations compared with the dispersion relations obtained with LSWT and ISWT (see text for details). The LMSWT and IMSWT results are not shown as their dispersions are virtually identical to that of LSWT and ISWT, respectively, except near $k = 0, \pm\pi/3$. The k quantum numbers have to be understood relative to the ground state quantum number. (b) Oscillator strength calculated with DDMRG (stars and numbers) compared with the intensity obtained from LSWT.

can be eliminated by introducing chemical potentials for each spin center, which result in finite excitation gaps for Goldstone modes (or the singlet-triplet gap) and thereby remove the divergencies. This branch of SWTs is denoted as modified SWTs,⁵⁷ the simplest of which is linear modified SWT (LMSWT),⁴⁶⁻⁴⁸ but also a number of interacting variants exist. Here we use full-diagonalization interacting modified SWT (IMSWT).⁴⁹ A conceptually different approach is to introduce Schwinger bosons and treat the resulting Hamiltonian at the mean-field level (Schwinger-boson mean field theory),^{50,51} which however yields exactly the same excitation spectrum as LMSWT and is hence not further considered here. For the $N = 8$, $s = 5/2$ system it was found that a simple correction of the LSWT spectrum, called LSWT+ Δ_c , gave the best agreement with the exact energies.¹⁸ In this approach, the first-order approximation $\Delta_c = 4J/N$ for the singlet-

TABLE I: (D)DMRG and SWT results for the ground-state energy E_g , singlet-triplet gap Δ , height of the dispersion curve, and mean deviation for a $N = 18$, $s = 5/2$ uniform AFM Heisenberg ring in units of J . The numerical inaccuracy of the DMRG ground state energy is two orders smaller than given.

	E_g/J	Δ/J	height/ J	χ^2
(D)DMRG	-129.703	0.2683(1)	5.50(1)	0
LSWT	-128.835	0	4.924	0.0602
LMSWT	-129.082	0.1228	4.926	0.0582
ISWT	-129.759	0	5.288	0.0246
IMSWT	-129.693	0.1319	5.289	0.0246
LSWT+ Δ_c		0.2222	5.146	0.0316
ISWT+ Δ_c		0.2222	5.511	0.0066

triplet gap (or $a_1 = a_1^{AB}$) is added to the excitation energies. We will additionally consider ISWT+ Δ_c , where the estimated gap is added to the spectrum of ISWT.

For these theories the ground-state and one-magnon energies can be calculated analytically for AFM wheels.⁴⁴⁻⁵¹ The resulting ground-state energies, singlet-triplet gaps, and maximal energies (= heights of the dispersion curves) are listed in Table I, which also presents the corresponding values for the one- J model Hamiltonian obtained from (D)DMRG, see appendix B. Furthermore the mean deviation of SWT and DDMRG excitation energies or $\chi^2 = \sum_k [\omega(k) - \omega_{\text{DDMRG}}(k)]^2 / (\frac{1}{2}NJs)$ is given. The excitation energies are also displayed in Fig. 10(a).

The trends for $N = 18$, $s = 5/2$ are similar to what has been observed for $N = 8$, $s = 5/2$:¹⁸ For the ground-state energy IMSWT provides the best approximation to the DMRG result. The singlet-triplet gap cannot be reproduced by LSWT and ISWT, in contrast to LMSWT and IMSWT. However, their predictions are about a factor two too small, and in particular significantly poorer than the simple estimate $\Delta_c = 4J/N$. The calculated excitations for LSWT and LMSWT are nearly identical as seen by similar mean deviations, as well as that for ISWT and IMSWT [LMSWT and IMSWT dispersion curves were hence not plotted in Fig. 10(a) for clarity]. Thus, as a conclusion, similar to the situation for $N = 8$, $s = 5/2$ wheels, IMSWT provides the best results also for $N = 18$, $s = 5/2$ wheels as regards the ground-state and E -band excitation energies, and the singlet-triplet gap is underestimated by about a factor of 2. The best description for the excitations is in fact provided by the simple LSWT+ Δ_c and ISWT+ Δ_c approaches, with a significant advantage of ISWT+ Δ_c (in contrast to the $N = 8$ ring, where LSWT+ Δ_c did better).

Besides the position of the energy levels also the oscillator strengths¹⁶ $|\langle S, M | \hat{S}^z(k) | S', M' \rangle|^2$ ($\hat{S}^z(k) = \sum_j \exp(-ikj) \hat{S}_j^z$) of the transitions from the ground state ($S = 0$) to the excited $S' = 1$ states were calculated for the uniform $N = 18$, $s = 5/2$ wheel using DDMRG.

The oscillator strength is not identical to the INS intensity for a specific transition, but both are intimately related.³⁶ The oscillator strengths are independent of specific INS-experiment parameters and are thus better suited for general discussions. The results are summarized in Fig. 10(b). As expected, the oscillator strengths increase with increasing k , becoming maximal at the zone boundary, reminiscent to the behavior of Goldstone modes at the Bragg points $k = \pi$ in infinite lattices. Interestingly, the oscillator strengths are well described, at least on the logarithmic scale used in Fig. 10(b), by the predictions of LSWT.⁵⁸ The LSWT result shows a divergency at the Bragg point $k = \pi$, which reflects the underlying assumption of a long-range Néel-ordered ground state or zero singlet-triplet gap, as discussed before several times. The good agreement of the DDMRG and LSWT oscillator strength provides a further strong indication that the elementary excitations in $N = 18$, $s = 5/2$ AFM wheels are indeed discrete spin-wave excitations, and for the validity of the $L&E$ -band picture.

V. CONCLUSIONS

In summary, we report a combined experimental and theoretical study of the magnetism in the antiferromagnetic molecular ferric wheel Fe_{18} . It is demonstrated that nowadays advanced experimental and theoretical tools such as inelastic neutron scattering, (dynamical) density matrix renormalization group techniques, and quantum Monte Carlo together with established methods such as spin-wave theory permit a detailed characterization of large magnetic molecules with huge Hilbert space dimensions, such as the molecular ferric wheel Fe_{18} . The combined approach allowed us to determine accurate magnetic parameters as well as to test and rationalize effective models such as the $L&E$ -band picture, which are of paramount importance for a deeper understanding of the physics in AFM wheels and quantum-spin clusters in the mesoscopic regime in general. The concrete result for the Fe_{18} wheel, whose size is situated at the border between microscopic and macroscopic, is that the higher-lying elementary excitations have the character of discrete antiferromagnetic spin waves.

Acknowledgments

The authors thank Eric Jeckelmann and Piet Dargel for discussions about the DDMRG technique. Funding by the Deutsche Forschungsgemeinschaft (FOR 945, SCHN 615/16-1, WAL 1524/5-1) and the USA National Science Foundation is thankfully acknowledged. N.B.I. is partially supported by the Bulgarian Science Foundation (Grant No. DO 02-264). This work is partially based on experiments performed at the Swiss spallation neutron source SINQ, Paul Scherrer Institute, Villigen, Switzerland.

Appendix A: Methods

1. Experimental Methods

The Fe_{18} material was synthesized according to the procedure described in the literature.¹³ The magnetic susceptibility data was recorded on a microcrystalline sample using a SQUID magnetometer (Quantum Design) in an applied field of 0.5 T. The data were corrected for the contribution of the sample holder. The sample was prepared by selecting sufficiently many single crystals from the mother liquor, squash them and mount them on the sample holder, and to cool the sample down as quickly as possible. This procedure typically minimizes contamination by magnetic impurities. INS spectra were recorded at the time-of-flight disc chopper spectrometer IN5 at the Institute Laue-Langevin (Grenoble, France) with incoming neutron wavelength $\lambda = 4.2 \text{ \AA}$ and at the direct time-of-flight spectrometer FOCUS at the Paul Scherrer Institut (Villigen, Switzerland) with incoming neutron wavelengths $\lambda = 3.2$ and 2.26 \AA . For each INS experiment a fresh non-deuterated powder sample of Fe_{18} was synthesized, and filled in a double-walled hollow aluminum can. The weight of the samples were approximately 0.5 and 1.8 g for the measurements at IN5 and FOCUS, respectively. All data were corrected for detector efficiency with a measurement of a vanadium standard. At FOCUS also empty can measurements were done and used for empty can corrections. Experimental resolutions at the elastic line were $165 \mu\text{eV}$ in the IN5 experiment, and 430 and $1100 \mu\text{eV}$ in the FOCUS experiments. If not stated otherwise, spectra were summed over all detector banks. Positive energies correspond to energy loss of the neutron.

2. Numerical Methods

The INS spectra were calculated as follows. The formula for the differential INS cross section of powder-averaged isotropic systems^{36,37,59} reads

$$\frac{d^2\sigma}{d\Omega d\omega} \propto \frac{k'}{k} e^{-2W} F^2(Q) S^{zz}(Q, \omega), \quad (\text{A1})$$

where $\mathbf{Q} = \mathbf{k} - \mathbf{k}'$ is the momentum transfer, e^{-2W} is the Debye-Waller factor, and $F(Q)$ is the magnetic form factor of Fe^{III} ions. The scattering function $S^{zz}(Q, \omega)$ is defined as

$$S^{zz}(Q, \omega) = \sum_{j,j'} \frac{\sin(QR_{jj'})}{QR_{jj'}} S_{jj'}^{zz}(\omega), \quad (\text{A2})$$

where $S_{jj'}^{zz}(\omega)$ is at zero temperature given by

$$S_{jj'}^{zz}(\omega) \equiv \sum_n \langle 0 | \hat{S}_j^z | n \rangle \langle n | \hat{S}_{j'}^z | 0 \rangle \delta(\hbar\omega - E_n + E_0). \quad (\text{A3})$$

For the calculation of $S_{jj'}^{zz}(\omega)$ the dynamical density-matrix renormalization group (DDMRG) technique was

used.^{30–32} Details of the calculation are given in Appendix B. Strictly speaking the molecule Fe_{18} is zero-dimensional, but effectively forms a one-dimensional chain with periodic boundary conditions and is hence suited for DDMRG. However, the calculations are nevertheless very time-consuming due to the applied periodic boundary conditions. For the calculations on the model with different coupling constants up to 600 density matrix eigenstates were kept. For the calculations on the uniform Heisenberg model up to 850 density matrix eigenstates were kept in order to achieve a smaller broadening η . The truncated weight depends on the energies $\hbar\omega$ as well as η , and ranged between 10^{-7} and 10^{-4} , which is a very large, but not unusual value for a DDMRG calculation, cf. Ref. 60. We checked the results for a different number of kept density matrix eigenstates and no significant changes of peak positions or heights were observed. For the direct calculation of the low-lying energy levels the ALPS DMRG code²⁶ was used, and up to 3000 density matrix eigenstates were kept.

The magnetization of Fe_{18} was evaluated by means of Quantum Monte Carlo (QMC) calculations^{24,25,54} employing again the ALPS code.²⁶ Since the underlying Hilbert space is huge, dimension $(2s + 1)^N = 101, 559, 956, 668, 416$, we used 10,000,000 sweeps for the thermalization and 10,000,000,000 sweeps for the evaluation of the magnetization for every value of the temperature.

All calculations were performed on a BULL supercomputer with 128 cores and 386 GB RAM running ScaleMP vsmp.

Appendix B: Dynamical DMRG

The basic steps of the DDMRG technique are briefly discussed. DDMRG^{30–32,61} is an extension of the standard DMRG method.^{27–29,62} It is a powerful numerical method for the calculation of zero temperature dynamical correlation functions such as (we set $\hbar = 1$ in this section)

$$G_{A,B}(\omega) = -\frac{1}{\pi} \langle 0 | \hat{A}^\dagger \frac{1}{E_0 + \omega + i\eta - \hat{H}} \hat{B} | 0 \rangle, \quad (\text{B1})$$

where $|0\rangle$ denotes the ground state with the energy E_0 . For the comparison to a spectroscopic experimental method such as inelastic neutron scattering, the important part of this function is the imaginary part (by setting $\hat{A} = \hat{S}_j^z$ and $\hat{B} = \hat{S}_{j'}^z$, one obtains the function $\text{Im} G_{A,B}(\omega) = S_{jj'}^{zz}(\omega)$, cf. Sec. A 2)

$$\text{Im} G_{A,B}(\omega) = \frac{1}{\pi} \langle A | \frac{\eta}{(E_0 + \omega - \hat{H})^2 + \eta^2} | B \rangle \quad (\text{B2})$$

$$= \sum_n \langle A | n \rangle \langle n | B \rangle \delta_\eta(\omega + E_0 - E_n), \quad (\text{B3})$$

where $\delta_\eta(x)$ is the Lorentzian broadened delta function with $\lim_{\eta \rightarrow 0} \delta_\eta(x) = \delta(x)$, and $|A\rangle \equiv \hat{A}|0\rangle$, $|B\rangle \equiv \hat{B}|0\rangle$.

E_n denotes the energy eigenvalue belonging to the eigenstate $|n\rangle$. A calculation of the matrix elements $\langle A|n\rangle$ by directly calculating the excited states $|n\rangle$ using standard DMRG is possible only for low energies since all energy eigenstates up to the desired state have to be included as target states in forming the reduced density matrix. Many target states, however, decrease the accuracy of a DMRG calculation.²⁷ The basic idea of the DDMRG method is a reformulation of this equation using the so-called correction vector, which is defined as³¹

$$|C(\omega)\rangle = \frac{1}{E_0 + \omega + i\eta - \widehat{H}}|B\rangle. \quad (\text{B4})$$

If one splits the correction vector into $|C(\omega)\rangle = |C^r(\omega)\rangle + i|C^i(\omega)\rangle$ with

$$|C^i(\omega)\rangle = \frac{1}{(E_0 + \omega - \widehat{H})^2 + \eta^2}|B\rangle \quad (\text{B5})$$

and

$$|C^r(\omega)\rangle = \frac{\widehat{H} - E_0 - \omega}{\eta}|C^i(\omega)\rangle, \quad (\text{B6})$$

a direct calculation of $\text{Im } G_{A,B}(\omega)$ is possible as

$$\text{Im } G_{A,B}(\omega) = \frac{1}{\pi} \langle A|C^i(\omega)\rangle. \quad (\text{B7})$$

$|C^i(\omega)\rangle$ is calculated as the solution of a linear equation system within the reduced DMRG basis. The target states for the reduced density matrix are $|0\rangle$, $|B\rangle$, $|C^i(\omega)\rangle$, and $|C^r(\omega)\rangle$. For $A = B$ a different calculation of $\text{Im } G_{A,B}(\omega)$ by reformulating (B5) as a minimization is also possible³² but we found no significant differences between the two approaches. For solving the linear equation system we use a simple CG algorithm.⁶³ DDMRG is a very time-consuming method because the calculation has to be repeated for every ω . However, since calculations for different ω are independent, this method is easy to parallelize.

To gain information about the one-magnon dispersion relation of the uniform chain we have calculated the dynamical correlation function $S^z(k, \omega)$, which is defined as

$$S^z(k, \omega) = \sum_{j,j'} e^{ik(j-j')} S_{jj'}^{zz}(\omega), \quad (\text{B8})$$

($k = 2\pi q/N$, $q = 0, 1, \dots, 17$) and can thus be obtained by simply Fourier transforming the $S_{jj'}^{zz}(\omega)$ data.⁶¹ A different way to calculate $S(k, \omega)$ is to set $\widehat{A} = \widehat{B} = \widehat{S}^z(k) \equiv \sum_j \exp(-ikj) \widehat{S}_j^z$ for the calculation of $\text{Im } G_{A,B}(\omega)$.³¹ However, with this procedure only excitations which contribute sufficiently to the dynamical correlation function can be detected. For the transition from the ground state to the lowest three $S = 1$ states it is also possible to directly calculate the transition matrix elements and the oscillator strengths using standard DMRG (cf. Ref. 64).

If possible, we have employed and compared all three approaches to obtain and validate the results shown in Fig. 10. However, the numbers shown in Fig. 10 are not numerically exact values. We estimate the relative errors of the oscillator strengths to be smaller than 10 % in all cases.

Appendix C: Spin-wave theory for the AFM $J_1 - J_2 - J_3$ Heisenberg Ring

The one-magnon spectrum of the isotropic Heisenberg ring Eq. (1) or three- J model was considered in a first-order (next to linear) SWT approximation. Since the unit cell of the model contains three half-integer spins with $s = 5/2$, the Lieb-Mattis theorem implies that the ground state in the case of AFM bonds is a singlet.^{65,66}

For the SWT calculations it is convenient to introduce spherical coordinates J_R , θ , and ϕ through the standard relations:

$$\begin{aligned} \frac{J_1}{J_R} &= \cos \phi \sin \theta \equiv x, \\ \frac{J_2}{J_R} &= \sin \phi \sin \theta \equiv y, \\ \frac{J_3}{J_R} &= \cos \theta \equiv z, \\ J_R &= \sqrt{J_1^2 + J_2^2 + J_3^2}, \end{aligned} \quad (\text{C1})$$

where $0 \leq \phi \leq \frac{\pi}{2}$ and $0 \leq \theta \leq \pi/2$ for AFM exchange constants. The radial coordinate J_R appears as an overall factor in the Hamiltonian, Eq. (1), and sets the energy scale. The spin operators were parameterized as follows:

$$\begin{aligned} \widehat{S}_{l,\alpha}^z &= \cos \Phi \left[s + \frac{1}{2} - \frac{1}{2}(\widehat{p}_{l,\alpha}^2 + \widehat{q}_{l,\alpha}^2) \right] - \sin \Phi \sqrt{S} \widehat{q}_{l,\alpha}, \\ \widehat{S}_{l,\alpha}^x &= \sin \Phi \left[s + \frac{1}{2} - \frac{1}{2}(\widehat{p}_{l,\alpha}^2 + \widehat{q}_{l,\alpha}^2) \right] + \cos \Phi \sqrt{S} \widehat{q}_{l,\alpha}, \\ \widehat{S}_{l,\alpha}^y &= \sqrt{S} \widehat{p}_{l,\alpha}, \end{aligned} \quad (\text{C2})$$

where $\alpha = 1, 2, 3$ and $l = 1, 2, \dots, L$. The angle Φ alternatively takes the two values 0 and π on the lattice sites along the ring. The coordinate $\widehat{q}_{l,\alpha}$ and momentum $\widehat{p}_{l,\alpha}$ satisfy the usual commutation relations $[\widehat{q}_{l,\alpha}, \widehat{p}_{l',\beta}] = i\delta_{l,l'}\delta_{\alpha,\beta}$.

In terms of the Fourier transforms

$$(\widehat{q}_{k,\alpha}, \widehat{p}_{k,\alpha}) = \frac{1}{\sqrt{L}} \sum_{l=1}^L (\widehat{q}_{l,\alpha}, \widehat{p}_{l,\alpha}) \exp(-ikl) \quad (\text{C3})$$

the linear spin-wave theory (LSWT) Hamiltonian reads

$$\widehat{H}_{LSWT} = E'_g + \frac{J_R s}{2} \sum_k (\widehat{\mathbf{p}}_{-k} \cdot \mathbf{M}_k \cdot \widehat{\mathbf{p}}_k + \widehat{\mathbf{q}}_{-k} \cdot \mathbf{N}_k \cdot \widehat{\mathbf{q}}_k), \quad (\text{C4})$$

where $E_g' = -J_R(x+y+z)s(s+1)L$, $\hat{\mathbf{q}}_k = (\hat{q}_{k,1}, \hat{q}_{k,2}, \hat{q}_{k,3})$ and $\hat{\mathbf{p}}_k = (\hat{p}_{k,1}, \hat{p}_{k,2}, \hat{p}_{k,3})$. The Hermitian matrices \mathbf{M}_k and \mathbf{N}_k read

$$M_k^{\alpha\beta} = \begin{pmatrix} x+z & x & z \exp(-3ik) \\ x & x+y & y \\ z \exp(3ik) & y & y+z \end{pmatrix}, \quad (\text{C5})$$

$$N_k^{\alpha\beta} = \begin{pmatrix} x+z & -x & -z \exp(-3ik) \\ -x & x+y & -y \\ -z \exp(3ik) & -y & y+z \end{pmatrix}. \quad (\text{C6})$$

The Hamilton equations of motion for the vectors $\hat{\mathbf{q}}_k$ and $\hat{\mathbf{p}}_k$ take the form

$$\frac{d\hat{\mathbf{q}}_k}{dt} = J_R s \mathbf{M}_k \hat{\mathbf{p}}_k, \quad (\text{C7})$$

$$\frac{d\hat{\mathbf{p}}_k}{dt} = -J_R s \mathbf{N}_k \hat{\mathbf{q}}_k, \quad (\text{C8})$$

which yield three spin-wave branches with dispersions $\omega_\alpha(k)$ defined by the secular cubic equation

$$\det \left(\mathbf{M}_k \cdot \mathbf{N}_k - \frac{\omega_\alpha(k)^2}{J_R^2 s^2} \mathbf{I} \right) = 0, \quad (\text{C9})$$

where \mathbf{I} is the unit (3×3) matrix. In diagonal form the spin-wave Hamiltonian \hat{H}_{LSWT} then becomes

$$\hat{H}_{LSWT} = E_g + \sum_{\alpha=1}^3 \sum_k \omega_\alpha(k) \hat{n}_{k,\alpha}, \quad (\text{C10})$$

where $\hat{n}_{k,\alpha}$ is the occupation number operator of the (k, α) state and E_g is the ground-state energy:

$$E_g = -\frac{J_1 + J_2 + J_3}{3} N s (s+1) + \frac{1}{2} \sum_{\alpha=1}^3 \sum_k \omega_\alpha(k). \quad (\text{C11})$$

It is useful to present the cubic equation for $\omega_\alpha(k)$ in the following dimensionless form

$$\xi^3 + a_2 \xi^2 + a_1 \xi + a_0 = 0, \quad (\text{C12})$$

with

$$\begin{aligned} a_0 &= -\frac{4x^2 y^2 z^2}{(xy + yz + zx)^3} \sin^2(3k), \\ a_1 &= 1, \\ a_2 &= -2. \end{aligned} \quad (\text{C13})$$

The spin-wave energies are related to the three roots $\xi_{k,\alpha}$ of Eq. (C12) by the expressions

$$\omega_\alpha(k) = \sqrt{J_1 J_2 + J_2 J_3 + J_3 J_1} s \left(1 + \frac{R}{s} \right) \sqrt{\xi_{k,\alpha}}. \quad (\text{C14})$$

Notice that in this expression the first-order correction to the one-magnon energies was introduced through Oguchi's renormalization factor R .⁴⁵ For the uniform ring or one- J model holds $R = 1/2 - 1/\pi \approx 0.1817$. In the general case, R is expected to be a smooth regular function of the parameters θ and ϕ . In principle, one can calculate this function in the next-order SWT. However, the correction is small (few %) and is hence not employed here. For the three- J model of Fe_{18} , the spin-wave excitations are distributed in five energy levels defined as follows:

$$\begin{aligned} L_0 &= \omega_1(0) = \omega_1(\pi/3), \\ E_1 &= \omega_1(\pm\pi/9) = \omega_1(\pm 2\pi/9), \\ E_2 &= \omega_2(\pm\pi/9) = \omega_2(\pm 2\pi/9), \\ E_3 &= \omega_2(0) = \omega_3(0) = \omega_2(\pi/3) = \omega_3(\pi/3), \\ E_4 &= \omega_3(\pm\pi/9) = \omega_3(\pm 2\pi/9). \end{aligned} \quad (\text{C15})$$

The degeneracies are dictated by the spatial C_6 symmetry plus the underlying bipartite sublattice structure.

Since the coefficient a_0 in Eq. (C12) vanishes for $k = 0$ and $\pm\pi/3$, the roots at these special points of the Brillouin zone can easily be determined to $\xi_1 = 0$, $\xi_{2,3} = 1$. In terms of the energy levels one hence finds $L_0 = 0$ and

$$E_3 = s \left(1 + \frac{R}{s} \right) \sqrt{J_1 J_2 + J_2 J_3 + J_3 J_1}, \quad (\text{C16})$$

and the energy E_3 plays the role of an overall prefactor in the dispersion of the magnon excitations since

$$\omega_\alpha(k) = E_3 \sqrt{\xi_{k,\alpha}}. \quad (\text{C17})$$

Actually, E_3 absorbs the explicit dependence on the parameters J_1 , J_2 and J_3 apart from the dependence of $\xi_{k,\alpha}$ through a_0 .

Useful relations between the energy levels E_1 , E_2 , E_3 , and E_4 follow from Viète's formulas at $k = \pi/9$: $\xi_{k,1} + \xi_{k,2} + \xi_{k,3} = -a_2 = 2$, $\xi_{k,1}\xi_{k,2} + \xi_{k,2}\xi_{k,3} + \xi_{k,3}\xi_{k,1} = a_1 = 1$, and $\xi_{k,1}\xi_{k,2}\xi_{k,3} = b_0$, where $b_0 \equiv -a_0(\pi/9)$. With Eqs. (C15) one obtains

$$\begin{aligned} 2E_3^2 &= E_1^2 + E_2^2 + E_4^2, \\ E_3^4 &= E_1^2 E_2^2 + E_2^2 E_4^2 + E_4^2 E_1^2, \\ b_0 E_3^6 &= E_1^2 E_2^2 E_4^2. \end{aligned} \quad (\text{C18})$$

Equations (C16) and (C18) are very handy to investigate the trends in the one-magnon spectrum with varying exchange constants J_1 , J_2 and J_3 , and led to a number of general conclusions which are useful for analyzing the INS peaks, see Sec. III B.

-
- ¹ K. Bärwinkel, H.-J. Schmidt, and J. Schnack, *J. Magn. Mater.* **220**, 227 (2000).
- ² K. L. Taft, C. D. Delfs, G. C. Papaefthymiou, S. Foner, D. Gatteschi, and S. J. Lippard, *J. Am. Chem. Soc.* **116**, 823 (1994).
- ³ R. W. Saalfrank, I. Bernt, E. Uller, and F. Hampel, *Angew. Chem. Int. Ed.* **36**, 2482 (1997).
- ⁴ S. P. Watton, P. Fuhrmann, L. E. Pence, S. J. Lippard, A. Caneschi, A. Cornia, and G. L. Abbati, *Angew. Chem. Int. Ed.* **36**, 2774 (1997).
- ⁵ A. Chiolero and D. Loss, *Phys. Rev. Lett.* **80**, 169 (1998).
- ⁶ G. Abbati, A. Caneschi, A. Cornia, A. Fabretti, and D. Gatteschi, *Inorganica Chimica Acta* **297**, 291 (2000).
- ⁷ J. van Slageren, R. Sessoli, D. Gatteschi, A. A. Smith, M. Helliwel, R. E. P. Winpenny, A. Cornia, A.-L. Barra, A. G. M. Jansen, E. Rentschler, et al., *Chem. Eur. J.* **8**, 277 (2002).
- ⁸ K. Bärwinkel, P. Hage, H.-J. Schmidt, and J. Schnack, *Phys. Rev. B* **68**, 054422 (2003).
- ⁹ O. Waldmann, *Coordin. Chem. Rev.* **249**, 2550 (2005).
- ¹⁰ O. Waldmann, T. Guidi, S. Carretta, C. Mondelli, and A. L. Dearden, *Phys. Rev. Lett.* **91**, 237202 (2003).
- ¹¹ E. Micotti, Y. Furukawa, K. Kumagai, S. Carretta, A. Lascialfari, F. Borsa, G. A. Timco, and R. E. P. Winpenny, *Phys. Rev. Lett.* **97**, 267204 (2006).
- ¹² N. Hoshino, M. Nakano, H. Nojiri, W. Wernsdorfer, and H. Oshio, *J. Am. Chem. Soc.* **131**, 15100 (2009).
- ¹³ P. King, T. C. Stamatatos, K. A. Abboud, and G. Christou, *Angew. Chem. Int. Ed.* **45**, 7379 (2006).
- ¹⁴ O. Waldmann, T. C. Stamatatos, G. Christou, H. U. Güdel, I. Sheikin, and H. Mutka, *Phys. Rev. Lett.* **102**, 157202 (2009).
- ¹⁵ J. Schnack and M. Luban, *Phys. Rev. B* **63**, 014418 (2000).
- ¹⁶ O. Waldmann, *Phys. Rev. B* **65**, 024424 (2002).
- ¹⁷ J. Schnack, M. Luban, and R. Modler, *Europhys. Lett.* **56**, 863 (2001).
- ¹⁸ J. Dreiser, O. Waldmann, C. Dobe, G. Carver, S. T. Ochsenein, A. Sieber, H. U. Güdel, J. van Duijn, J. Taylor, and A. Podlesnyak, *Phys. Rev. B* **81**, 024408 (2010).
- ¹⁹ O. Waldmann, *Phys. Rev. B* **75**, 012415 (2007).
- ²⁰ R. Schnalle and J. Schnack, *Int. Rev. Phys. Chem.* **29**, 403 (2010).
- ²¹ C. Delfs, D. Gatteschi, L. Pardi, R. Sessoli, K. Wieghardt, and D. Hanke, *Inorg. Chem.* **32**, 3099 (1993).
- ²² O. Waldmann, *Phys. Rev. B* **61**, 6138 (2000).
- ²³ B. Pilawa, R. Boffinger, I. Keilhauer, R. Leppin, I. Odenwald, W. Wendl, C. Berthier, and M. Horvatic, *Phys. Rev. B* **71**, 184419 (2005).
- ²⁴ A. W. Sandvik and J. Kurkijärvi, *Phys. Rev. B* **43**, 5950 (1991).
- ²⁵ A. W. Sandvik, *Phys. Rev. B* **59**, R14157 (1999).
- ²⁶ A. Albuquerque, F. Alet, P. Corboz, P. Dayal, A. Feiguin, S. Fuchs, L. Gamper, E. Gull, S. Gürtler, A. Honecker, et al. (ALPS collaboration), *J. Magn. Mater.* **310**, 1187 (2007), see also <http://alps.comp-physics.org>.
- ²⁷ S. R. White, *Phys. Rev. B* **48**, 10345 (1993).
- ²⁸ U. Schollwöck, *Rev. Mod. Phys.* **77**, 259 (2005).
- ²⁹ S. R. White, *Phys. Rev. Lett.* **69**, 2863 (1992).
- ³⁰ S. Ramasesha, S. K. Pati, H. R. Krishnamurthy, Z. Shuai, and J. L. Brédas, *Synth. Met.* **85**, 1019 (1997), ISSN 0379-6779.
- ³¹ T. D. Kühner and S. R. White, *Phys. Rev. B* **60**, 335 (1999).
- ³² E. Jeckelmann, *Phys. Rev. B* **66**, 045114 (2002).
- ³³ O. Waldmann, J. Schülein, R. Koch, P. Müller, I. Bernt, R. W. Saalfrank, H. P. Andres, H. U. Güdel, and P. Al-lenspach, *Inorg. Chem.* **38**, 5879 (1999).
- ³⁴ S. T. Ochsenein, F. Tuna, M. Rancan, R. S. G. Davies, C. A. Muryn, O. Waldmann, R. Bircher, A. Sieber, G. Carver, H. Mutka, et al., *Chem. Eur. J.* **14**, 5144 (2008).
- ³⁵ S. Stuiber, G. Wu, J. Nehrkor, J. Dreiser, Y. Lan, G. Novitchi, C. E. Anson, T. Unruh, A. K. Powell, and O. Waldmann, *Chem. Eur. J.* **17**, 9094 (2011).
- ³⁶ O. Waldmann, *Phys. Rev. B* **68**, 174406 (2003).
- ³⁷ A. Furrer, J. Mesot, and T. Strässle, *Neutron Scattering in Condensed Matter Physics* (World Scientific Publishing Co., 2009).
- ³⁸ S. Carretta, J. van Slageren, T. Guidi, E. Livioti, C. Mondelli, D. Rovai, A. Cornia, C. F. Dearden, A. L., M. Affronte, C. D. Frost, et al., *Phys. Rev. B* **67**, 094405 (2003).
- ³⁹ O. Waldmann, C. Dobe, H. Mutka, A. Furrer, and H. U. Güdel, *Phys. Rev. Lett.* **95**, 057202 (2005).
- ⁴⁰ P. Santini, S. Carretta, G. Amoretti, T. Guidi, R. Caciuffo, A. Caneschi, D. Rovai, Y. Qiu, and J. R. D. Copley, *Phys. Rev. B* **71**, 184405 (2005).
- ⁴¹ O. Waldmann, C. Dobe, H. U. Güdel, and H. Mutka, *Phys. Rev. B* **74**, 054429 (2006).
- ⁴² H.-J. Schmidt, J. Schnack, and M. Luban, *Phys. Rev. B* **64**, 224415 (2001).
- ⁴³ N. B. Ivanov and D. Sen, *Spin Wave Analysis of Heisenberg Magnets in Restricted Geometries* (Springer, Berlin, Heidelberg, 2004), vol. 645 of *Lecture Notes in Physics*, chap. Molecular Magnetism, pp. 195–226.
- ⁴⁴ P. W. Anderson, *Phys. Rev.* **86**, 694 (1952).
- ⁴⁵ T. Oguchi, *Phys. Rev.* **117**, 117 (1960).
- ⁴⁶ M. Takahashi, *Phys. Rev. B* **40**, 2494 (1989).
- ⁴⁷ J. E. Hirsch and S. Tang, *Phys. Rev. B* **40**, 4769 (1989).
- ⁴⁸ S. Tang, M. E. Lazzouni, and J. E. Hirsch, *Phys. Rev. B* **40**, 5000 (1989).
- ⁴⁹ S. Yamamoto and H. Hori, *Journal of the Physical Society of Japan* **72**, 769 (2003).
- ⁵⁰ A. Auerbach and D. P. Arovos, *Phys. Rev. Lett.* **61**, 617 (1988).
- ⁵¹ S. Sarker, C. Jayaprakash, H. R. Krishnamurthy, and M. Ma, *Phys. Rev. B* **40**, 5028 (1989).
- ⁵² B. Gu, G. Su, and S. Gao, *Phys. Rev. B* **73**, 134427 (2006).
- ⁵³ O. Waldmann, *Europhys. Lett.* **60**, 302 (2002).
- ⁵⁴ L. Engelhardt and M. Luban, *Phys. Rev. B* **73**, 054430 (2006).
- ⁵⁵ M. Troyer, *Lecture Notes in Computer Science* **1732**, 164 (1999).
- ⁵⁶ O. Waldmann, R. Koch, S. Schromm, J. Schülein, P. Müller, I. Bernt, R. W. Saalfrank, F. Hampel, and E. Balthes, *Inorg. Chem.* **40**, 2986 (2001).
- ⁵⁷ M. Takahashi, *Phys. Rev. Lett.* **58**, 168 (1987).
- ⁵⁸ G. Müller, *Phys. Rev. B* **26**, 1311 (1982).
- ⁵⁹ O. Waldmann and H. U. Güdel, *Phys. Rev. B* **72**, 094422 (2005).
- ⁶⁰ S. Nishimoto and M. Arikawa, *Phys. Rev. B* **79**, 113106 (2009).
- ⁶¹ A. Honecker, S. Hu, R. Peters, and J. Richter, *J. Phys.: Condens. Matter* **23**, 164211 (2011).

- ⁶² M. Exler and J. Schnack, Phys. Rev. B **67**, 094440 (2003).
- ⁶³ D. Yang, *C++ and Object-oriented Numeric Computing for Scientists and Engineers* (Springer Verlag, New York Berlin Heidelberg, 2000).
- ⁶⁴ I. Schneider, A. Struck, M. Bortz, and S. Eggert, Phys. Rev. Lett. **101**, 206401 (2008).
- ⁶⁵ E. H. Lieb, T. Schultz, and D. C. Mattis, Ann. Phys. (N.Y.) **16**, 407 (1961).
- ⁶⁶ E. H. Lieb and D. C. Mattis, J. Math. Phys. **3**, 749 (1962).